

Generation of out-of-plane polarized spin current by spin swapping

Binoy K. Hazra^{1,†}, Banabir Pal^{1,†}, Jae-Chun Jeon¹, Robin R. Neumann², Borge Göbel², Bharat Grover¹, Hakan Deniz¹, Andriy Styervoyedov¹, Holger Meyerheim¹, Ingrid Mertig², See-Hun Yang¹, Stuart S. P. Parkin^{1,*}

¹*Max Planck Institute of Microstructure Physics, Weinberg 2, 06120 Halle (Saale), Germany*

²*Institut für Physik, Martin-Luther-Universität Halle-Wittenberg, D-06099 Halle (Saale), Germany*

[†]These authors contributed equally to this work.

*To whom correspondence should be addressed: stuart.parkin@halle-mpi.mpg.de

The generation of spin currents and their application to the manipulation of magnetic states is fundamental to spintronics. Of particular interest are chiral antiferromagnets that exhibit properties typical of ferromagnetic materials even though they have negligible magnetization. Here, we report the generation of a robust spin current with both in-plane and out-of-plane spin polarization in epitaxial thin films of the chiral antiferromagnet Mn_3Sn in proximity to permalloy thin layers. By employing temperature-dependent spin-torque ferromagnetic resonance, we find that the chiral antiferromagnetic structure of Mn_3Sn is responsible for an in-plane polarized spin current that is generated from the interior of the Mn_3Sn layer and whose temperature dependence follows that of this layer's antiferromagnetic order. On the other hand, the out-of-plane spin polarized spin current is unrelated to the chiral antiferromagnetic structure and is instead the result of scattering from the Mn_3Sn /permalloy interface. We substantiate the later conclusion by performing studies with several other non-magnetic metals all of which are found to exhibit out-of-plane polarized spin currents arising from the spin swapping effect.

Introduction

The Spin Hall effect (SHE)¹⁻⁴ allows for the generation of spin currents from charge currents that are passed through the interior of thin metallic layers. The magnitude and polarization direction of the spin current are widely inferred from the spin-torque ferromagnetic resonance technique (ST-FMR)⁵⁻⁸ in which the spin current is used to provide torques on proximal ferromagnetic layers. The polarization of the spin current is typically observed to lie in the plane⁹ of the metallic layer but the quest for out-of-plane polarized spin currents¹⁰⁻¹⁸ has attracted much attention as they could be used to manipulate perpendicularly magnetized layers without any external magnetic field, an essential ingredient for spintronic applications.

The polarization direction of the spin current in conventional non-magnetic metals is always even under a magnetic field, but it has been predicted that currents passed through non-collinear antiferromagnet (AFM), such as the Mn_3X ($X= Sn, Ir$), can give rise to additional spin currents that are odd under magnetic field^{19,20}. Subsequently, a dominant odd magnetic SHE with an out-of-plane spin-polarization along with a small even conventional SHE was inferred in single crystals of Mn_3Sn from spin-pumping and ST-FMR experiments^{21,22}. Although the magnetic SHE has been argued to be one of the fundamental mechanisms to generate out-of-plane polarized spin current in non-collinear antiferromagnetic thin films^{23,24}, but it's direct correlation with the antiferromagnetic order parameter by temperature dependence studies has not yet been established.

Here, we explore the SHE generated in high-quality epitaxial thin films of Mn_3Sn (0001) via studies of the spin-orbit torque (SOT) on thin epitaxial layers of ferromagnet permalloy ($Ni_{80}Fe_{20} = Py$), which are grown on top of the Mn_3Sn layers. We observe robust in-plane (p_y) and out-of-plane (p_z) polarized spin currents for various thicknesses of Mn_3Sn when a charge current

is passed through the Mn₃Sn/Py device (Fig. 1e). These give rise to large in-plane anti-damping-like and in-plane field-like torques with comparable magnitudes, respectively. Both p_y and p_z retain the same magnitude and sign when large in-plane magnetic fields are applied to reverse the AFM structure of the Mn₃Sn layer. By performing temperature-dependent ST-FMR, we demonstrate that p_y strongly depends on the AFM structure whereas p_z is unrelated to the antiferromagnetic ordering of Mn₃Sn, rather it originates from the scattering at the Py interface. We further substantiate the origin of p_z by measurements on various non-magnetic metals (Cu, Ru, Re and Pt)/Py bilayers with different strengths of bulk spin-orbit coupling (SOC). Based on these experimental results, we demonstrate that this interface-scattered p_z originates from the *spin swapping* mechanism²⁵⁻²⁹.

Results and Discussion

Mn₃Sn crystallizes in a hexagonal DO_{19} crystal structure with a kagome inverse triangular antiferromagnetic spin configuration within the (0001) plane (Fig. 1a) that is a result of the interplay between the geometric frustration of the spins coupled by Heisenberg exchange interaction and the Dzyaloshinskii-Moriya interaction. A small single-ion anisotropy results in a small in-plane moment³⁰, which allows for an external magnetic field to set the AFM structure in a specific domain structure. Epitaxial thin films of Mn₃Sn with thicknesses (d_{AFM}) ranging from 3 nm to 12 nm were grown on Ru buffered Al₂O₃(0006) substrates using an ultra-high vacuum d.c. magnetron sputtering. A 5 nm thick Ni₈₀Fe₂₀ (Py) layer was sputtered on top of the Mn₃Sn layer and capped with a 3 nm thick TaN layer (see Methods). Figure 1b shows typical X-ray diffraction (XRD) patterns of two representative samples with 3 nm and 12 nm thick Mn₃Sn layers. The (0002) and (0004) reflections from Ru and Mn₃Sn establish their epitaxial growth along (0001)

which is further confirmed by transverse phi (ϕ) scans of the Al_2O_3 $\{10\bar{1}4\}$, Ru $\{10\bar{1}2\}$ and Mn_3Sn $\{20\bar{2}1\}$ reflections (Fig. 1c). A detailed structural analysis confirms that the crystal symmetry of Mn_3Sn belongs to $\text{P}\bar{6}_3/\text{mmc}$ (see section I, Supplementary Information (SI)). Atomic force micrographs display a smooth surface of all films with a typical roughness of ~ 0.5 nm (Fig. S4a in SI). Transmission electron microscopy imaging confirms the high quality of the film structure (Fig. S4b in SI).

The properties of Ru/ Mn_3Sn /TaN films grown without any Py layer were investigated by magnetization and transport measurements. A small magnetization within the kagome plane (0001) is observed when an in-plane magnetic field is used to orient the AFM into a single domain. The magnitude of this magnetization is consistent with the expected chiral AFM structure of Mn_3Sn thin film³¹ and, moreover, decreases as the temperature is increased close to the Néel temperature (Fig. S5a in SI). Again consistent with prior work³² no anomalous Hall effect is observed when the current is applied within the kagome plane (Fig. S6b in SI).

The ST-FMR technique as shown in Fig. 1d was used to measure SOTs in devices formed from the Ru(5 nm)/ Mn_3Sn (d_{AFM})/Py(5 nm) structures (hereinafter referred to as $\text{Mn}_3\text{Sn}/\text{Py}$) which were fabricated to allow for the RF current (I_{RF}) to be oriented along two distinct in-plane crystallographic directions. The devices were prepared by standard optical lithography and a lift-off technique was used to prepare the Ti/Au electrical contacts (see Methods). I_{RF} gives rise to a d.c. mixing voltage, V_{mix} , that is measured when a magnetic field is swept through the resonance condition for the Py. V_{mix} is given by the equation^{5,8},

$$V_{\text{mix}} = V_0 \left[V_S \frac{\Delta H^2}{\Delta H^2 + (H_{\text{ext}} - H_{\text{res}})^2} + V_A \frac{\Delta H (H_{\text{ext}} - H_{\text{res}})}{\Delta H^2 + (H_{\text{ext}} - H_{\text{res}})^2} \right] \quad (1)$$

where V_0 is a constant pre-factor, V_S and V_A are the amplitudes of a symmetric and antisymmetric Lorentzian, respectively, H_{res} is the resonance field, ΔH is the linewidth and H_{ext} is the external magnetic field. First, we consider what we name the “0°” device in which I_{RF} is along the in-plane crystallographic direction $[01\bar{1}0]$ of Mn_3Sn . V_{mix} is measured as a function of φ , the angle between I_{RF} and H_{ext} . V_S and V_A are extracted by fitting $V_{\text{mix}}(\varphi)$ with equation (1). V_S is nearly zero at $\varphi = 150^\circ, 220^\circ$ as compared to $\varphi = 330^\circ, 40^\circ$, whereas the magnitude of V_A is the same at all of these φ (see Fig. 2(a-d) for $d_{\text{AFM}} = 12$ nm). Thus $V_S(\varphi)$ displays a very different angular variation compared to $V_A(\varphi)$ (Fig. 3(a,b) for $d_{\text{AFM}} = 12$ nm). Similar results are found for all d_{AFM} (Fig. S8 in SI). By fitting $V_S(\varphi)$ and $V_A(\varphi)$ to the following equations¹³, the in-plane and out-of-plane SOTs can be extracted:

$$V_S(\varphi) = -A(\tau_{x,\text{AD}} \sin \varphi \sin 2\varphi + \tau_{y,\text{AD}} \cos \varphi \sin 2\varphi + \tau_{z,\text{FL}} \sin 2\varphi) \quad (2)$$

$$V_A(\varphi) = -A \sqrt{1 + M_{\text{eff}}/H_{\text{res}}} (\tau_{x,\text{FL}} \sin \varphi \sin 2\varphi + \tau_{y,\text{FL}} \cos \varphi \sin 2\varphi + \tau_{z,\text{AD}} \sin 2\varphi) \quad (3)$$

where $A = -\frac{I_{\text{RF}}}{2} \frac{1}{\alpha(2\mu_0 H_{\text{res}} + \mu_0 M_{\text{eff}})}$ is a constant. $\tau_{i,\text{AD}}$ and $\tau_{i,\text{FL}}$ correspond to anti-damping-like and field-like torques resulting from p_i ($i = x, y, z$), the components of polarization of the spin current along x, y, and z. We find that $\tau_{x,\text{AD}}$ and $\tau_{x,\text{FL}}$ due to p_x and, $\tau_{z,\text{AD}}$ due to p_z are negligibly small whereas the magnitudes of $\tau_{y,\text{AD}}/\tau_{y,\text{FL}}$ and $\tau_{z,\text{FL}}/\tau_{y,\text{FL}}$ are large and nearly equal. Note that $\tau_{y,\text{AD}}$ and $\tau_{z,\text{FL}}$ are normalized to $\tau_{y,\text{FL}}$, which is dominated by oersted field, for ease of comparison with other systems that we discuss later. Hereinafter, $\tau_{y,\text{AD}}/\tau_{y,\text{FL}}$ and $\tau_{z,\text{FL}}/\tau_{y,\text{FL}}$ are referred to as $\tau'_{y,\text{AD}}$ and $\tau'_{z,\text{FL}}$, respectively. Note that the effective magnetization which is used to calculate the torques, is independent of d_{AFM} (Fig. S7b in SI). We also note that the addition of a spin-pumping contribution³³ to $\tau_{y,\text{AD}}$ does not reproduce the unusual variation of $V_S(\varphi)$ (Fig. S8 in SI). The

directions of $\tau_{y,AD}$, $\tau_{y,FL}$ and $\tau_{z,FL}$ are shown schematically in Fig. 2e for several φ . The torques $\tau_{z,FL}$ and $\tau_{y,AD}$ are oriented along the same direction for $\varphi = 330^\circ$ and 40° whereas they are oriented in opposite directions for $\varphi = 150^\circ$ and 220° which results in the unusual variation of $V_S(\varphi)$. In the second set of “90°” devices I_{RF} is along the in-plane crystallographic direction $[2\bar{1}\bar{1}0]$ of Mn_3Sn (Fig. 3c,d). Note that the angle between the $[2\bar{1}\bar{1}0]$ and $[01\bar{1}0]$ directions is 90° . $\tau'_{y,AD}$ remains unchanged whereas $\tau'_{z,FL}$ is reduced to a small but non-zero value. Previously, it has been shown in other materials that p_z displays a cosine angular dependence as a function of φ when p_z originates due to either low crystal symmetry or low magnetic symmetry^{10,14,15}. Theoretically, the same cosine angular dependence of the p_z is also calculated for Mn_3Sn assuming a chiral AFM structure (see section VI in SI). Thus, the finite $\tau'_{z,FL}$ that we measure for the 90° device necessitates a distinct origin for p_z .

We find that neither $\tau'_{y,AD}$ nor $\tau'_{z,FL}$ has a significant dependence on d_{AFM} , which suggests that they arise from the interface between Mn_3Sn and Py (Fig. 4a,c) or, equivalently, that the spin diffusion length in Mn_3Sn is small³⁴. The 6-fold symmetry of the AFM structure of Mn_3Sn means that there are six equivalent magnetic ground states³⁵. The AFM structure of Mn_3Sn can be set in a single domain state (or its twin) by applying a sufficiently large in-plane positive (or negative) magnetic field³⁶. Here using $H_{set} = \pm 7$ T at 300 K we find, however, that $V_S(\varphi)$ and $V_A(\varphi)$ remain the same (Fig. S9 in SI). Consequently, the strength of $\tau'_{y,AD}$ and $\tau'_{z,FL}$ are unchanged for the twin AF domains which shows that both p_y and p_z are even under magnetic field. Since thickness and external magnetic field dependence of SOTs do not provide an insight into the mechanism of p_y and p_z , we explore the temperature dependence of the SOTs close to the Néel-temperature of Mn_3Sn ($T_N = 420$ K). Interestingly, we find that $\tau'_{y,AD}$ is significantly reduced with

increase in temperature (Fig. 4b). This is a clear evidence that $\tau'_{y,AD}$ is directly related to the AFM structure of Mn_3Sn . With increase in temperature, AFM domains start to fluctuate which causes a reduction in $\tau'_{y,AD}$. Although p_y arises from the AFM structure, it shows thickness independent behaviour due to the small spin diffusion length of Mn_3Sn ³⁴. On the other hand, $\tau'_{z,FL}$ remains unchanged in the temperature range of 300-400 K (Fig. 4b) which implies that $\tau'_{z,FL}$ is unrelated to AFM structure of Mn_3Sn . The temperature and thickness independent behaviour of $\tau'_{z,FL}$ indicates the interfacial origin of p_z which is distinct compared to recent reports on non-collinear AFM Mn_3GaN ¹³.

To investigate how the $\text{Mn}_3\text{Sn}/\text{Py}$ interface influences p_z , we modified the interface by inserting a 2 nm thick Cu layer. The shape of $V_S(\varphi)$ and the strength of $\tau'_{y,AD}$ and $\tau'_{z,FL}$ remain similar to the structure without the Cu insertion layer (Fig. S13 in SI). This is because $\tau_{y,AD}$ is negligibly small in Cu. On the other hand, $\tau_{y,AD}$ is large in Pt and indeed when a Pt layer (2 nm thick) is inserted the shape of $V_S(\varphi)$ is significantly modified (Fig. S15e in SI). We also find that $\tau'_{y,AD}$ is enhanced due to the additional $\tau_{y,AD}$ from Pt, but $\tau'_{z,FL}$ remains almost unchanged (Fig. S15g,h in SI). The fact that $\tau'_{z,FL}$ is nearly equal for both 2 nm Cu and Pt insertion layers showing that the Py plays a key role in generating p_z .

Based on our experimental results, we propose that the generation of p_z which is controlled by the proximal ferromagnet (here Py) can be understood from the *spin swapping* mechanism²⁵⁻²⁹. The spin-polarized currents (along 'x') from the proximal in-plane magnetized layer (Py) are reflected from the interface (here interface between Mn_3Sn and Py) and, simultaneously, precess in the presence of an interfacial spin-orbit field (lower panel in Fig. 1e). After the precession, the

primary spin-polarized current generates a secondary spin current with out-of-plane spin polarization, p_z which successively induces substantial field-like torque.

The *spin swapping* effect is differentiated by the presence of a large $\tau_{z,FL}$ -like torque as opposed to the $\tau_{y,AD}$ -like torque due to an SHE. The ratio $\tau_{y,AD}/\tau_{z,FL}$ thus indicates the dominant mechanism whether arising from spin swapping or an SHE. To corroborate this, we have replaced Mn_3Sn with various non-magnetic metals with a wide range of SOC strengths which includes Cu, Ru, Re, and Pt with the expectation that as the SOC increases the nature of the torque will show a crossover from a pure *spin swapping* regime to an SHE dominating regime. In our experiments, indeed we find that $\tau_{y,AD}/\tau_{z,FL}$ is minimal for small SOC metals such as Cu and Ru (Fig. 4d). On the other hand, heavy metals such as Re and Pt display a significant $\tau_{y,AD}/\tau_{z,FL}$ due to the dominance of an SHE. Interestingly, we find that Mn_3Sn lie in the transition region between these two mechanisms in which both the SHE and *spin swapping* effects are equally important such that the ratio $\tau_{y,AD}/\tau_{z,FL}$ is close to unity (Fig. 4d). Even though $\tau_{y,AD}/\tau_{z,FL}$ increases monotonically with SOC, the magnitude of $\tau'_{z,FL}$ is almost independent of the SOC (Fig. 4c), indicating that the spin-swapping effect is constant for the elements considered, even though they are very different transition metals. This independent behaviour of $\tau'_{z,FL}$ further shows that the generation of p_z is controlled by the proximal Py layer. On the other hand, the SHE causes an enhancement of $\tau'_{y,AD}$ as a function of their SOC (Fig. 4a) which results in a monotonic increase of $\tau_{y,AD}/\tau_{z,FL}$. Furthermore, theoretical predictions also show that the creation of p_z via a *spin swapping* process is more effective when disorder at the interface is reduced. Indeed, we find that $\tau_{z,FL}$ almost vanishes when Pt/Py is grown on Si/SiO₂ with a lower degree of crystallinity whereas $\tau_{z,FL}$ remains

finite when highly crystalline Pt/Py is grown on an (0006) oriented Al_2O_3 single crystalline substrate (Fig. S14 and S3 in SI).

Conclusion

In summary, we have shown the presence of robust and thickness independent p_y and p_z in $\text{Mn}_3\text{Sn}/\text{Py}$ bilayers. From their temperature dependence, we have demonstrated that p_y originates from the AFM structure of Mn_3Sn whereas p_z is unrelated to the AFM structure and is generated at the Py interface. Moreover, the observation of p_z when Mn_3Sn is replaced by several different non-magnetic metals i.e., Cu, Ru, Re and Pt is consistent with an interfacial origin by a spin swapping mechanism. This work provides insights into the origin of unconventional spin polarizations not only in chiral non-collinear antiferromagnets but also in various non-magnetic metals. Our observation of interface-scattered p_z will further enrich the field of spin-orbitronics.

Methods

Sample preparation: All the thin-films were grown by DC magnetron sputtering in an ultra-high vacuum system with a base pressure of 1×10^{-9} Torr. Atomically flat $\text{Al}_2\text{O}_3(0006)$ substrates were prepared by a wet etching procedure followed by a heat treatment at 1200°C for 4 hours. A 5 nm thick Ru buffer layer was first sputtered onto an $\text{Al}_2\text{O}_3(0006)$ substrate at ambient temperature using a sputtering power of 15 W and an Ar pressure of 3 mTorr. The Mn_3Sn layer was formed by co-sputtering of Mn and Sn from elemental sputter targets onto the Ru(0002) buffer layer at 200°C and at an Ar pressure of 3 mTorr. An optimized composition of $\text{Mn}_{3.1}\text{Sn}$ was used where the excess Mn helps to stabilize the hexagonal $D0_{19}$ phase. The sputtering powers were of 43 W and 8 W, respectively, for Mn and Sn. The Mn_3Sn layer thickness was varied from 3 to 12 nm. Cu, Ru, Pt and Re films, with layer thicknesses of ~ 5 nm were grown at room temperature

directly onto $\text{Al}_2\text{O}_3(0006)$ substrates using sputtering powers of 30 W, 15 W, 30 W and 30 W, respectively and at an Ar pressure of 3 mTorr. A 5 nm thick $\text{Ni}_{80}\text{Fe}_{20}$ (Py) layer was sputtered on top of Mn_3Sn and other non-magnetic metals with a sputtering power of 30 W and an Ar pressure of 3 mTorr. Also, Pt(5 nm)/Py(5 nm) was sputtered on Si(001)/ $\text{SiO}_2(25 \text{ nm})$ at room temperature. All the films were capped with a 3 nm thick TaN layer to prevent oxidation.

Device fabrication: The films were patterned into ST-FMR devices (Fig. 1d) oriented along different crystallographic directions with device lengths (75 μm) and widths (25 μm) using conventional photolithography techniques (365 nm maskless laser writer; MLA150, Heidelberg). Etching was carried out using Ar ion beam milling and in-situ secondary ion mass spectroscopy was used for end point detection. Electrical contacts were formed using magnetron sputtered Ti (2 nm) / Au (100 nm) bilayers.

Sample characterization: Rutherford backscattering (RBS) was used to determine the composition of Mn_3Sn film. The crystal structure of the films was characterized using a Bruker D8 Discover diffractometer with $\text{Cu K}\alpha$ source and Gallium-Jet X-ray source. Atomic force microscopy measurements were performed to probe the surface topography. A FEI TITAN 80–300 transmission electron microscope (TEM) with a probe corrector was used at an accelerating voltage of 300 kV for scanning TEM studies. The magnetic properties of films were characterized using a Quantum Design MPMS3 SQUID magnetometer. Temperature-dependent measurements of the longitudinal resistivity and the anomalous Hall resistivity were carried out in a Quantum Design Physical Property Measurement System (PPMS). Spin-orbit torques were measured using a home-made spin-torque ferromagnetic resonance set-up at 300 K and another set-up in a Lake-Shore probe station for temperature dependence measurements in the range of 300 K-400 K.

ST-FMR measurements: In the ST-FMR measurements, an RF current (I_{RF}) with power of 21 dBm at different frequencies was applied and the in-plane magnetic field was swept between 1200 Oe to 0. V_{mix} at $\varphi = 45^\circ$ was measured at different frequencies to calculate M_{eff} and Gilbert damping constant. Using M_{eff} and H_{res} for a particular frequency ($f = 8$ GHz), the strengths of individual torques are calculated from the fit of $V_S(\varphi)$ and $V_A(\varphi)$ using Eq.(2,3). Note that we did not evaluate the constant ‘A’ as all the torques are finally normalized by $\tau_{y,FL}$ for ease comparison. For the temperature dependence, the temperature was stabilized at a particular temperature then the angular dependence was carried out to evaluate the torques.

Supplementary information

Supplementary information for this article is available online.

Acknowledgements

SSPP acknowledges funding from the European Union’s Horizon 2020 research and innovation program under grant agreement no. 766566 (ASPIN), the Alexander von Humboldt Foundation in the framework of the Alexander von Humboldt Professorship endowed by the Federal Ministry of Education and Research, and the Deutsche Forschungsgemeinschaft (DFG, German Research Foundation) – project no. 403505322, Priority Program (SPP) 2137. I.M. acknowledges support from the DFG under SFB TRR 227.

Author Contributions

S.S.S.P conceived the project. B.K.H prepared the samples with the help of A.S. B.P and J.C.J fabricated the devices. B.K.H and B.P carried out all the experiments with help of J.C.J and B.Gr. B.K.H, B.P and S.H.Y analyzed the data. H.D performed TEM experiments. H.M carried out crystallographic symmetry analysis. R.R.N, B. Gö and I.M performed theoretical calculations. All authors discussed the results. B.K.H, B.P and S.S.S.P wrote the manuscript with substantial contributions from all authors.

References

- 1 Hirsch, J. E. Spin Hall Effect. *Phys. Rev. Lett.* **83**, 1834-1837 (1999).
- 2 Zhang, S. Spin Hall Effect in the Presence of Spin Diffusion. *Phys. Rev. Lett.* **85**, 393-396 (2000).
- 3 Sinova, J. *et al.* Universal Intrinsic Spin Hall Effect. *Phys. Rev. Lett.* **92**, 126603 (2004).
- 4 Valenzuela, S. O. & Tinkham, M. Direct electronic measurement of the spin Hall effect. *Nature* **442**, 176-179 (2006).
- 5 Tulapurkar, A. A. *et al.* Spin-torque diode effect in magnetic tunnel junctions. *Nature* **438**, 339-342 (2005).
- 6 Sankey, J. C. *et al.* Measurement of the spin-transfer-torque vector in magnetic tunnel junctions. *Nat. Phys.* **4**, 67-71 (2008).
- 7 Kubota, H. *et al.* Quantitative measurement of voltage dependence of spin-transfer torque in MgO-based magnetic tunnel junctions. *Nat. Phys.* **4**, 37-41 (2008).
- 8 Liu, L., Moriyama, T., Ralph, D. C. & Buhrman, R. A. Spin-Torque Ferromagnetic Resonance Induced by the Spin Hall Effect. *Phys. Rev. Lett.* **106**, 036601 (2011).
- 9 Manchon, A. *et al.* Current-induced spin-orbit torques in ferromagnetic and antiferromagnetic systems. *Rev. Mod. Phys.* **91**, 035004 (2019).
- 10 MacNeill, D. *et al.* Control of spin-orbit torques through crystal symmetry in WTe₂/ferromagnet bilayers. *Nat. Phys.* **13**, 300-305 (2017).
- 11 Guimarães, M. H. D., Stiehl, G. M., MacNeill, D., Reynolds, N. D. & Ralph, D. C. Spin-Orbit Torques in NbSe₂/Permalloy Bilayers. *Nano Lett.* **18**, 1311-1316 (2018).
- 12 Zhou, J. *et al.* Large spin-orbit torque efficiency enhanced by magnetic structure of collinear antiferromagnet IrMn. *Sci. Adv.* **5**, eaau6696 (2019).
- 13 Nan, T. *et al.* Controlling spin current polarization through non-collinear antiferromagnetism. *Nat. Commun.* **11**, 4671 (2020).
- 14 Bai, H. *et al.* Control of spin-orbit torques through magnetic symmetry in differently oriented noncollinear antiferromagnetic Mn₃Pt. *Phys. Rev. B* **104**, 104401 (2021).
- 15 You, Y. *et al.* Cluster magnetic octupole induced out-of-plane spin polarization in antiperovskite antiferromagnet. *Nat. Commun.* **12**, 6524 (2021).
- 16 Chen, X. *et al.* Observation of the antiferromagnetic spin Hall effect. *Nat. Mat.* **20**, 800-804 (2021).
- 17 Bose, A. *et al.* Tilted spin current generated by the collinear antiferromagnet ruthenium dioxide. *Nat. Electron.* **5**, 267-274 (2022).
- 18 Bai, H. *et al.* Observation of Spin Splitting Torque in a Collinear Antiferromagnet RuO₂. *Phys. Rev. Lett.* **128**, 197202 (2022).
- 19 Železný, J., Zhang, Y., Felser, C. & Yan, B. Spin-Polarized Current in Noncollinear Antiferromagnets. *Phys. Rev. Lett.* **119**, 187204 (2017).
- 20 Mook, A., Neumann, R. R., Johansson, A., Henk, J. & Mertig, I. Origin of the magnetic spin Hall effect: Spin current vorticity in the Fermi sea. *Phys. Rev. Res.* **2**, 023065 (2020).
- 21 Kimata, M. *et al.* Magnetic and magnetic inverse spin Hall effects in a non-collinear antiferromagnet. *Nature* **565**, 627-630 (2019).

- 22 Kondou, K. *et al.* Giant field-like torque by the out-of-plane magnetic spin Hall effect in a
topological antiferromagnet. *Nat. Commun.* **12**, 6491 (2021).
- 23 Holanda, J. *et al.* Magnetic Damping Modulation in IrMn₃/Ni₈₀Fe₂₀ via the Magnetic Spin
Hall Effect. *Phys. Rev Lett.* **124**, 087204 (2020).
- 24 Hu, S. *et al.* Efficient perpendicular magnetization switching by a magnetic spin Hall effect
in a noncollinear antiferromagnet. *Nat. Commun.* **13**, 4447 (2022).
- 25 Lifshits, M. B. & Dyakonov, M. I. Swapping Spin Currents: Interchanging Spin and Flow
Directions. *Phys. Rev. Lett.* **103**, 186601 (2009).
- 26 Saidaoui, H. B. M., Otani, Y. & Manchon, A. Crossover between spin swapping and Hall
effect in disordered systems. *Phys. Rev. B* **92**, 024417 (2015).
- 27 Saidaoui, H. B. M. & Manchon, A. Spin-Swapping Transport and Torques in Ultrathin
Magnetic Bilayers. *Phys. Rev. Lett.* **117**, 036601 (2016).
- 28 Park, H.-J. *et al.* Spin Swapping Effect of Band Structure Origin in Centrosymmetric
Ferromagnets. *Phys. Rev. Lett.* **129**, 037202 (2022).
- 29 Lin, W. *et al.* Evidence for spin swapping in an antiferromagnet. *Nature Physics* **18**, 800-
805 (2022).
- 30 Tomiyoshi, S. & Yamaguchi, Y. Magnetic Structure and Weak Ferromagnetism of Mn₃Sn
Studied by Polarized Neutron Diffraction. *J. Phys. Soc. Jap.* **51**, 2478-2486 (1982).
- 31 Markou, A. *et al.* Noncollinear antiferromagnetic Mn₃Sn films. *Phys. Rev. Mater.* **2**,
051001 (2018).
- 32 Nakatsuji, S., Kiyohara, N. & Higo, T. Large anomalous Hall effect in a non-collinear
antiferromagnet at room temperature. *Nature* **527**, 212-215 (2015).
- 33 Sklenar, J. *et al.* Driving and detecting ferromagnetic resonance in insulators with the spin
Hall effect. *Phys. Rev. B* **92**, 174406 (2015).
- 34 Muduli, P. K. *et al.* Evaluation of spin diffusion length and spin Hall angle of the
antiferromagnetic Weyl semimetal Mn₃Sn. *Phys. Rev. B* **99**, 184425 (2019).
- 35 Liu, J. & Balents, L. Anomalous Hall Effect and Topological Defects in Antiferromagnetic
Weyl Semimetals: Mn₃Sn/Ge. *Phys. Rev. Lett.* **119**, 087202 (2017).
- 36 Pal, B. *et al.* Setting of the magnetic structure of chiral kagome antiferromagnets by a
seeded spin-orbit torque. *Science Advances* **8**, eabo5930 (2022).

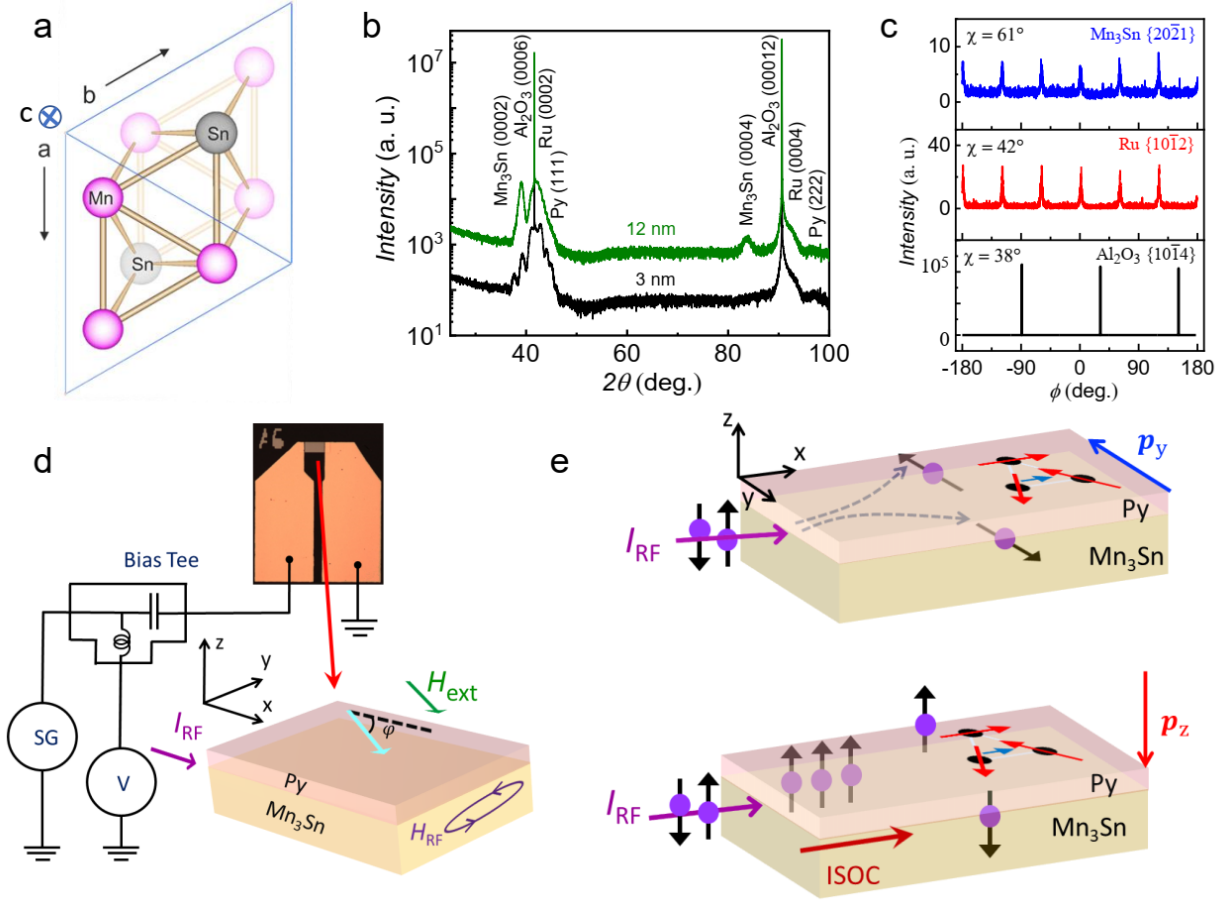


Fig. 1: X-ray diffraction, schematic of ST-FMR set-up and origin of spin polarizations. **a** Structure of Mn₃Sn viewed along the [0001] direction. Pink and grey balls represent Mn and Sn atoms, respectively. **b** X-ray diffraction pattern of Ru/Mn₃Sn(0001)/Py structures grown on Al₂O₃(0006) substrates. Mn₃Sn layer thicknesses are 3 nm (black) and 12 nm (green). **c** Phi (ϕ) scan across the Al₂O₃ {10 $\bar{1}$ 4}, Ru {10 $\bar{1}$ 2} and Mn₃Sn {20 $\bar{2}$ 1} reflections for the Ru/Mn₃Sn (0001)/Py structures with 12 nm Mn₃Sn film. **d** Schematic of ST-FMR experimental set-up and Mn₃Sn/Py device. The directions of I_{RF} , H_{ext} and angle (ϕ) between I_{RF} and H_{ext} are also shown. **e** The direction and origin of p_y and p_z for Mn₃Sn/Py structure are shown schematically. Upper panel shows that p_y originates from SHE which is related to AFM structure of Mn₃Sn. The p_z arises when the spin-polarized current from Py is scattered at the interface due to spin swapping effect (lower panel). Note that $\mathbf{p}_i = p_i \hat{i}$ ($i = y$ or z). The interfacial spin-orbit field is also shown schematically.

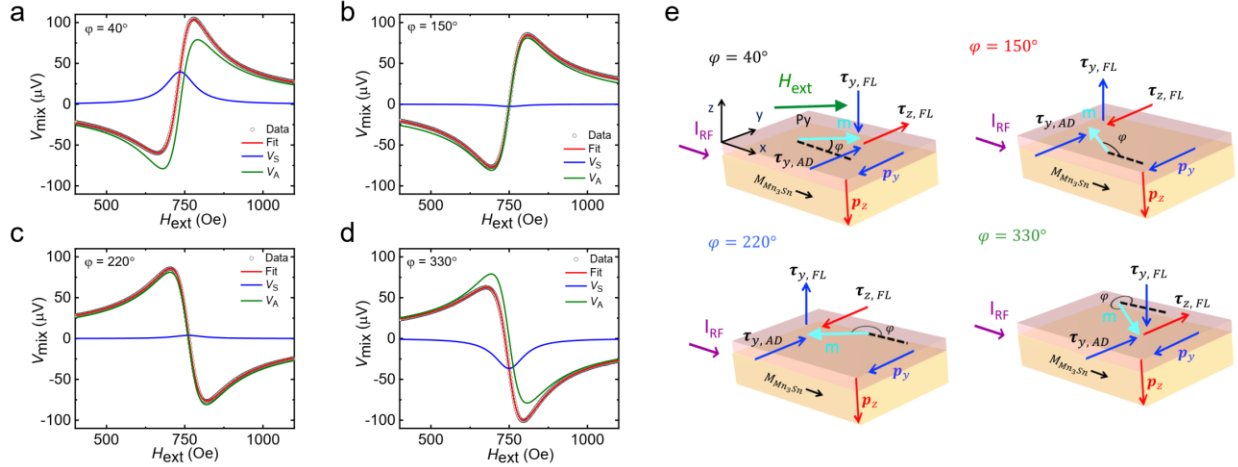


Fig. 2: ST-FMR d.c. voltage for different in-plane angles and torques directions. a-d ST-FMR d.c. voltages, V_{mix} , along with the fits based on Eq. 1 are shown for the pristine $\text{Mn}_3\text{Sn}(12 \text{ nm})/\text{Py}(5 \text{ nm})$ structures at $\varphi = 40^\circ, 150^\circ, 220^\circ$ and 330° , respectively. The individual V_S and V_A contributions are also plotted in the same figures. e Schematic illustration of p_y and p_z and respective torques due to these polarizations at the same φ . The vector form of $\tau_{y,AD}$, $\tau_{y,FL}$ and $\tau_{z,FL}$ are $(\mathbf{m} \times (\mathbf{m} \times \mathbf{p}_y))$, $(\mathbf{m} \times \mathbf{p}_y)$ and $(\mathbf{m} \times \mathbf{p}_z)$, respectively where \mathbf{m} is the magnetization of Py and $\mathbf{p}_i = p_i \hat{i}$ ($i = y$ or z). The torques $\tau_{z,FL}$ and $\tau_{y,AD}$ are oriented along the same direction for $\varphi = 330^\circ$ and 40° whereas they are oriented in opposite directions for $\varphi = 150^\circ$ and 220° . Note that the in-plane moment of Mn_3Sn remains in the same direction for various φ during ST-FMR measurements.

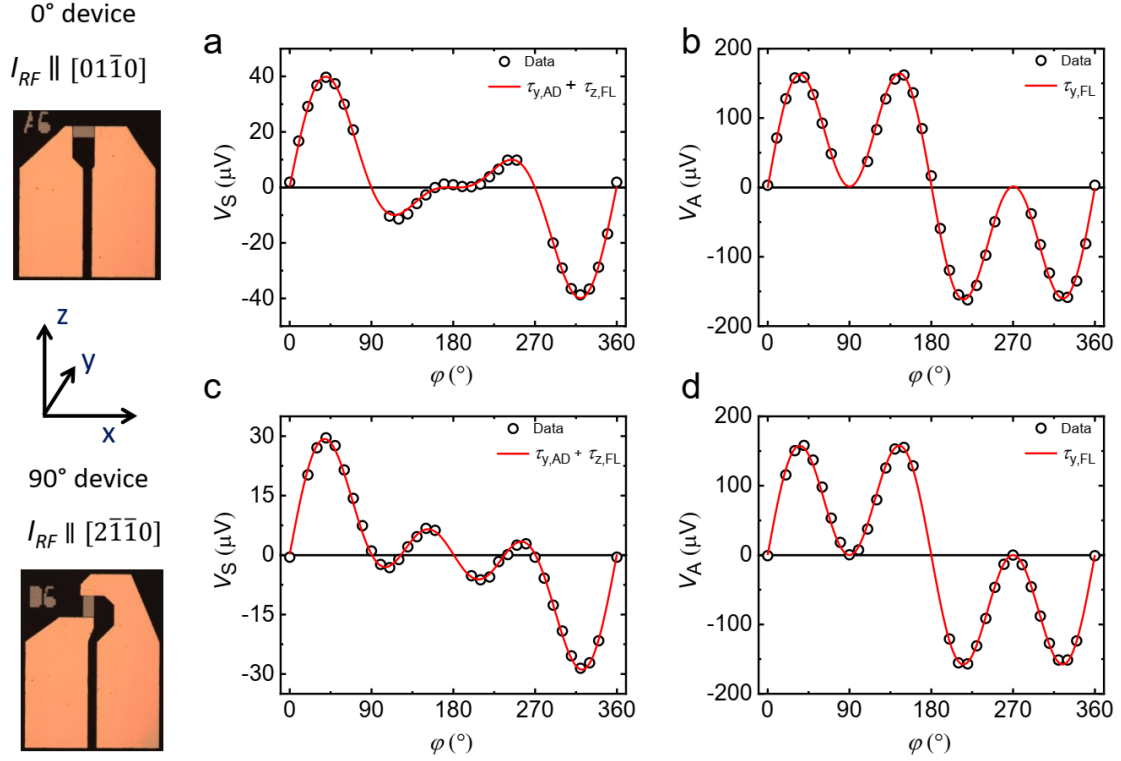


Fig. 3: Angular variation of V_S and V_A for two different devices. **a-b** Angular variation of V_S and V_A along with the fits based on Eq.(2-3) are shown in the range of 0° to 360° for the $\text{Mn}_3\text{Sn}(12 \text{ nm})/\text{Py}(5 \text{ nm})$ film. Here I_{RF} is along the in-plane crystallographic direction $[01\bar{1}0]$ of Mn_3Sn . **c-d** Angular variation of V_S and V_A along with the fits are shown for the 90° device where I_{RF} is along the in-plane crystallographic direction $[2\bar{1}\bar{1}0]$ of Mn_3Sn . The optical images of both the devices are also shown.

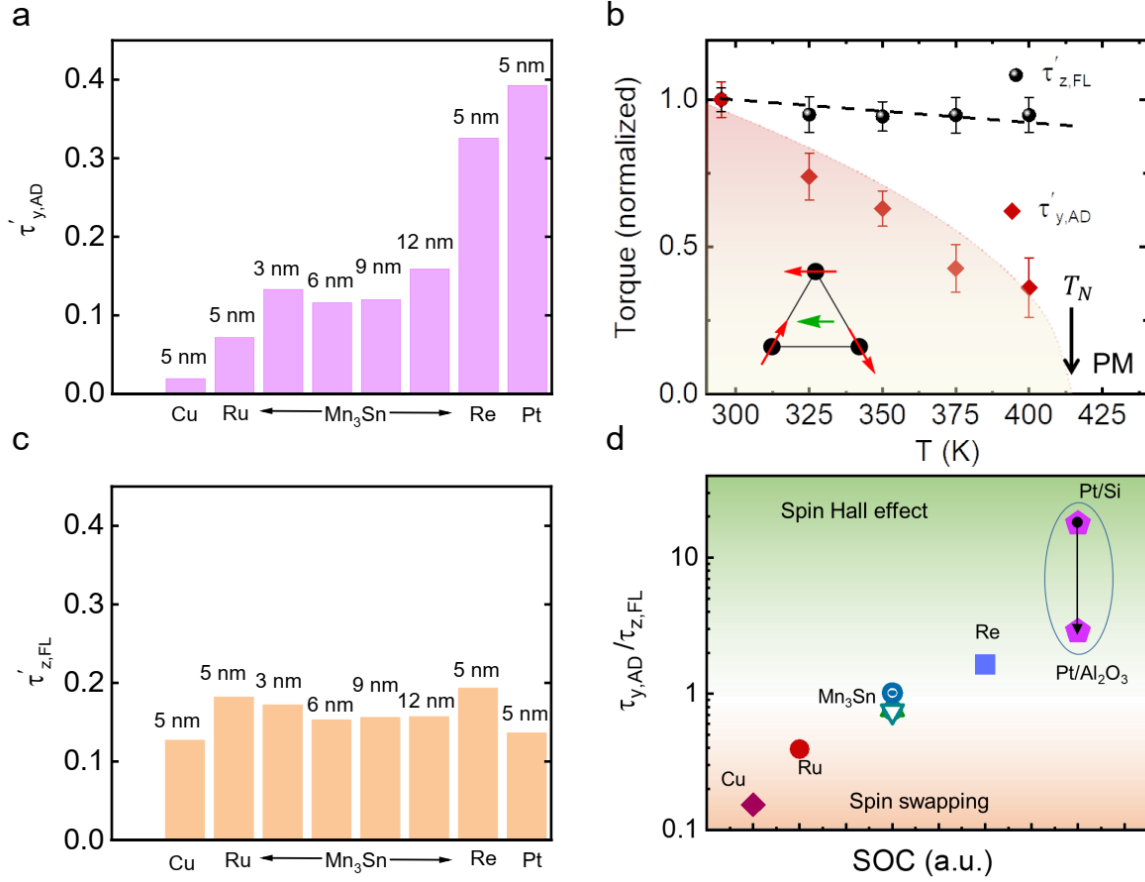


Fig. 4: Normalized torques, their temperature dependence and determination of SHE and spin swapping contribution. **a,c** $\tau'_{y,AD}$ ($\tau_{y,AD}/\tau_{y,FL}$) and $\tau'_{z,FL}$ ($\tau_{z,FL}/\tau_{y,FL}$) for Cu(5 nm)/Py(5 nm), Ru(5 nm)/Py(5 nm), Mn₃Sn (d_{AFM} =3-12 nm)/Py(5 nm), Re(5 nm)/Py(5 nm) and Pt(5 nm)/Py(5 nm) films which are grown on Al₂O₃ substrate. **b** Temperature dependence of $\tau'_{y,AD}$ and $\tau'_{z,FL}$ for the Mn₃Sn(12 nm)/Py(5 nm) film. **d** $\tau_{y,AD}/\tau_{z,FL}$ as a function of SOC for Mn₃Sn/Py and non-magnetic (Cu, Ru, Re and Pt)/Py bilayers. Spin swapping dominates for Cu and Ru whereas Mn₃Sn lies in between SHE and spin swapping effect. SHE dominates when Pt/Py is grown on Si/SiO₂ and spin swapping starts to make a significant contribution when the same structure is grown on Al₂O₃ substrates (data points with magenta color).